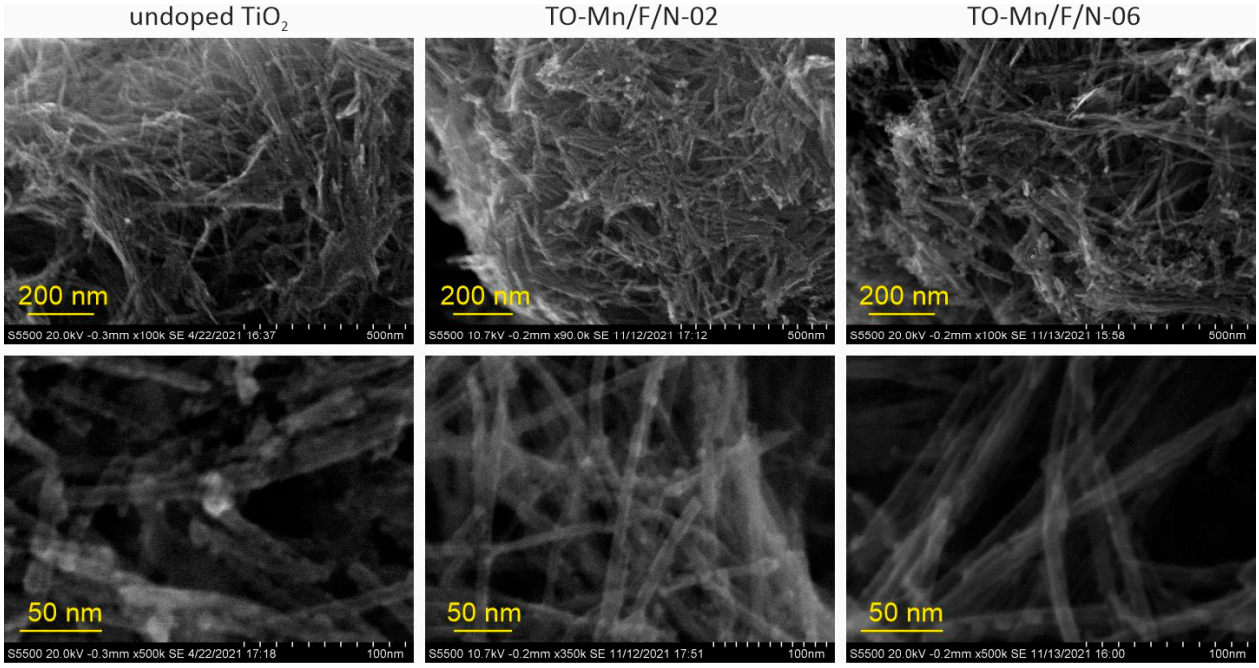

Figure S1. SEM-micrographs for the undoped TiO_2, TO-Mn/F/N-02 and TO-Mn/F/N-06 products

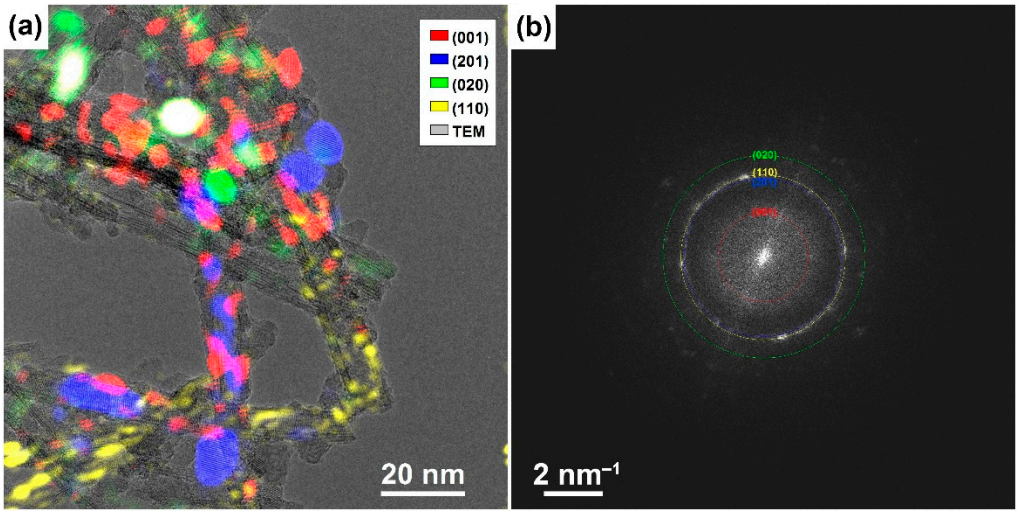

Figure S2. (a) Crystallographic orientation of TiO_2(B) crystals determined by HRTEM imaging in the TO-Mn/F/N-04 sample and (b) corresponding Fast Fourier Transform pattern

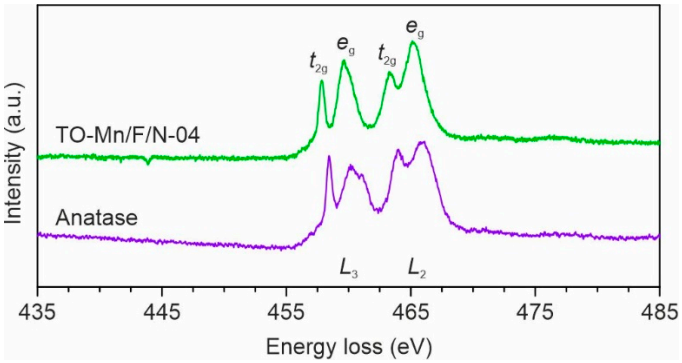

Figure S3. Experimental EELS spectra of Ti $L_{2,3}$-edges for the for the TO-Mn/F/N-04 sample and the commercial anatase TiO_2 examined for comparison

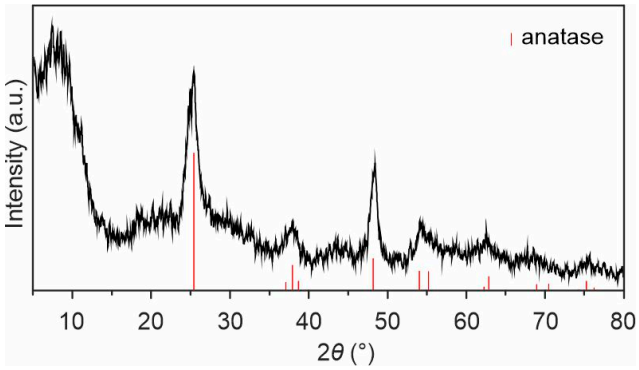

Figure S4. XRD pattern of product doped with 4 at.% Mn, synthesized without NH_4HF_2 (Bruker D8Advance diffractometer, CuK_α-radiation)

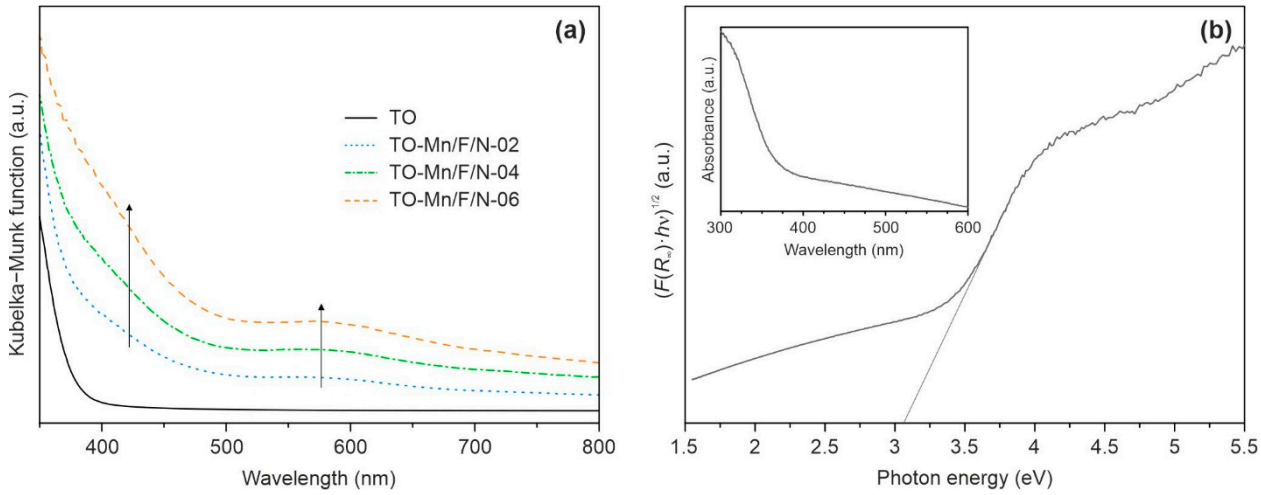

Figure S5. (a) UV-vis diffuse reflectance spectra represented as Kubelka-Munk function against wavelength plots for the undoped TiO_2, TO-Mn/F/N-02, TO-Mn/F/N-04, and TO-Mn/F/N-06 products and (b) Tauc plot for the (F, N) co-doped TiO_2 with the corresponding UV-vis absorption curve (inset)

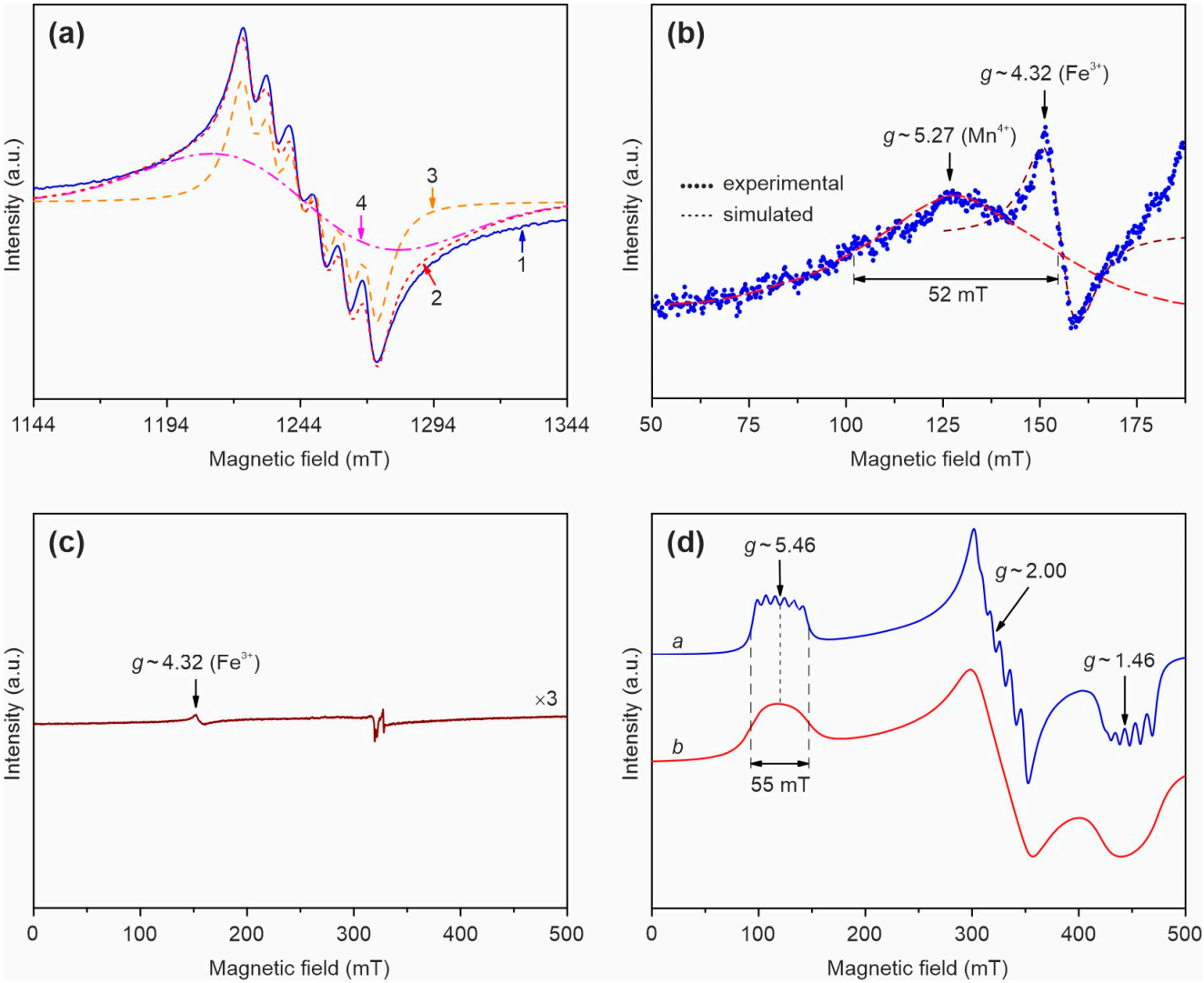

Figure S6. (a) Approximation (1) of the experimental Q-band EPR spectrum of the TO-Mn/F/N-04 sample at room temperature (2) by the sum of the spectrum with a sextet structure (3) and a single line with a Gaussian contour (4), (b) low field region of the X-band EPR spectrum at –160 °C, (c) the X-band EPR spectrum of undoped titanium dioxide, (d) simulated X-band EPR spectra of Mn^{4+} ions in the crystal fields with strong rhombic distortion; spectra "*a*" and "*b*" differ in the width (ΔB) of the hyperfine structure lines (see Table S4)

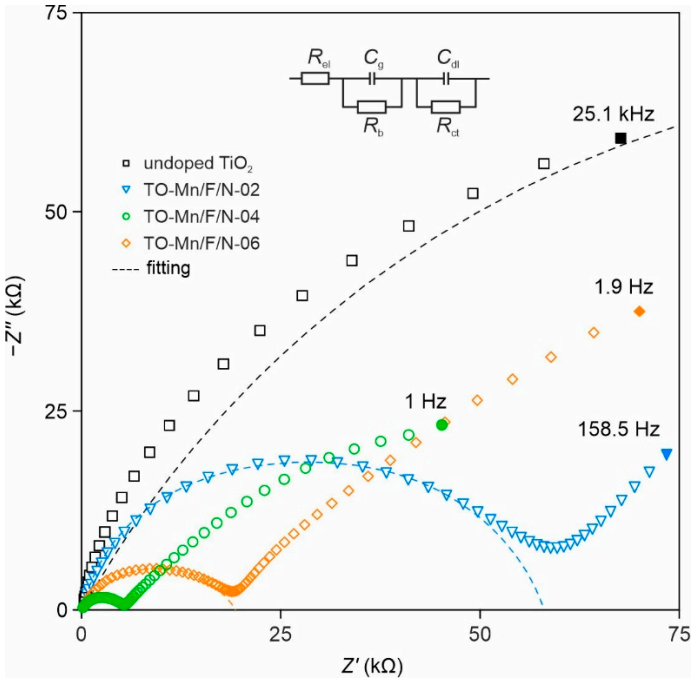

Figure S7. Zoom-in impedance spectra of the undoped TiO_2, TO-Mn/F/N-02, TO-Mn/F/N-04, and TO-Mn/F/N-06 materials and the EEC (inset) used for fitting

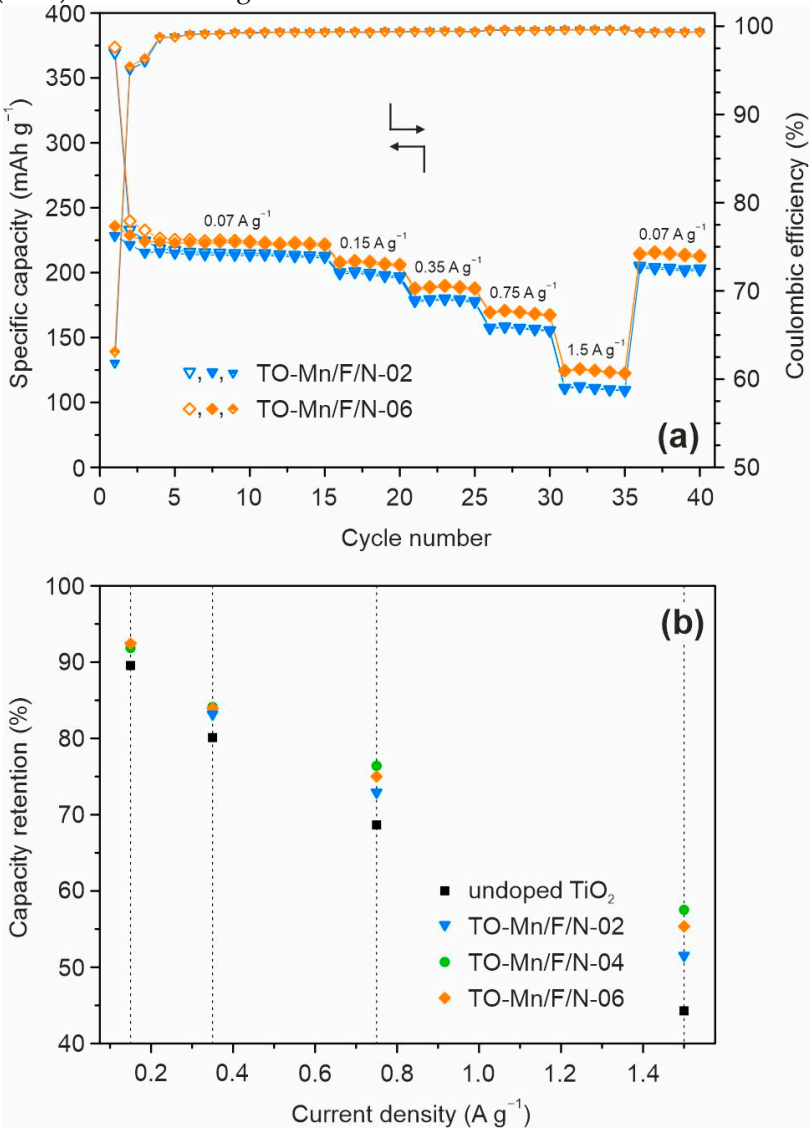

Figure S8. (a) Evolution of capacity during cycling under various current loads for TO-Mn/F/N-02 and TO-Mn/F/N-06 electrodes, (b) capacity retention at various current densities as compared to that at 70 mA g^{-1} for undoped TiO_2, TO-Mn/F/N-02, TO-Mn/F/N-04, and TO-Mn/F/N-06 materials

Table S1. Specific surface area, total pore volume, band gap energy, and conductivity of TiO_2 samples co-doped with Mn, F, and N as compared to an unmodified one

Sample	Specific surface area ($m^2\ g^{-1}$)*	Total pore volume ($cm^3\ g^{-1}$)*	Band gap energy (eV)	Conductivity ($S\ cm^{-1}$)
Undoped TiO_2	145.6	0.99	3.14	$2.9 \cdot 10^{-7}$
TO-F/Mn-02	197.7	0.91	2.45	$2.3 \cdot 10^{-6}$
TO-F/Mn-04	188.9	0.87	2.27	$5.7 \cdot 10^{-6}$
TO-F/Mn-06	203.0	0.88	2.00	$4.0 \cdot 10^{-6}$

* The surface area and total pore volume were determined by the density functional theory equation.

Table S2. Quantification results obtained by XPS analysis for the TO-Mn/F/N-06 sample

	Ti $2p_{3/2}$	O 1*s*	Mn $2p_{3/2}$	F 1*s*	N 1*s*	C 1*s*
Binding energy (eV)	456.5; 458.7	529.6; 532.1	641.6; 643.8	683.9; 688.6	400.1	285; 286.3; 289
Content (at.%)	27.9	58.2	1.3	2.7	0.8	9.1

Table S3. The Riveted refinement results for structures existed in unmodified and (Mn, F, N) co-doped TiO_2 samples

Sample	TiO_2(B)					Anatase		
	a (Å)	*b* (Å)	*c* (Å)	β (°)	*V* (Å^3)	*a* (Å)	*c* (Å)	*V* (Å^3)
Undoped TiO_2	12.1192(8)	3.7591(2)	6.5229(4)	107.55(1)	283.34(2)	3.7616(1)	9.384(4)	132.77(3)
TO-Mn/F/N-02	12.1909(7)	3.7427(2)	6.6435(4)	110.192(8)	284.49(2)	3.7586(4)	9.401(1)	132.80(3)
TO-Mn/F/N-04	12.2562(6)	3.7569(3)	6.6692(4)	110.896(9)	286.89(3)	3.7710(1)	9.438(2)	134.21(2)
TO-Mn/F/N-06	12.2431(7)	3.7545(4)	6.7258(7)	111.45(1)	287.74(3)	3.7750(1)	9.4457(2)	134.61(3)

Table S4. Spin Hamiltonian parameters used to simulate the EPR spectra of Mn^{4+} ions in crystal fields with strong rhombic distortion

Spectrum	*g*-factor	*E*/*D*	*A* (MHz)	Δ*B* (MHz)
a	2.00	1/3	245	5.4
b	2.00	1/3	245	23

The spin Hamiltonian in the calculations had the following form: $\hat{H}=g\beta(\vec{B},\vec{S})+D\left(\hat{S}_z^2-\frac{S(S+1)}{3}\right)+E\left(\hat{S}_x^2-\hat{S}_y^2\right)+A(\vec{I},\vec{S})$, where β is the Bohr magneton, $\vec{B}$ is the applied magnetic field, g is the spectroscopic splitting factor, $\vec{S}$ is the vector of the spin angular momentum of the system, $\hat{S}_x$, $\hat{S}_y$ и $\hat{S}_z$ – spin angular momentum operators along the x, y, and z axes, respectively, S is the spin value, D and E are the axial and rhombic components of the crystal field, respectively, $\vec{I}$ is the nuclear spin angular momentum vector, A is the constant of hyperfine structure (HFS). The calculations were performed under the assumption that E and $D >> g\beta|\vec{B}|$. The shape of the individual HFS line was Lorentzian.

Table S5. Calculated EIS parameters for unmodified and (Mn, F, N) co-doped TiO_2 samples

Sample	R_{el} (Ω)*	R_b (kΩ)	C_g		χ^2
			Q_g (S cm^{-1} s^n)	n	
Undoped TiO_2	83.26	223.59±2.79	(1.57±0.02)·10^{-9}	0.717±0.001	0.0019348
TO-Mn/F/N-02	83.26	52.02±0.81	(3.3±0.3)·10^{-10}	0.87±0.01	0.000733
TO-Mn/F/N-04	83.26	5.26±0.07	(1.27±0.14)·10^{-8}	0.686±0.007	0.00036213
TO-Mn/F/N-06	83.26	16.83±0.28	(4.37±0.43)·10^{-9}	0.71±0.01	0.00040345

* When fitting the R_{el} values were fixed at 83.26 Ω for all samples.

Table S6. Electrochemical performance of the doped TiO_2(B) anodes in lithium-ion batteries

Material	Initial charge/discharge capacity	Cycling performance	Rate capability	Reference (year)
Fe-doped TiO_2(B) nanorods[#]	490/219 mAh g^{-1} at 33.5 mA g^{-1}	170 mAh g^{-1} after 15 cycles at 33.5 mA g^{-1}	163 mAh g^{-1} at 1675 mA g^{-1}	[1] (2015)
Ca-doped TiO_2(B) thin films	293/226 mAh g^{-1} at 335 mA g^{-1}	102 mAh g^{-1} after 200 cycles at 26,800 mA g^{-1}	248 mAh g^{-1} at 3350 mA g^{-1}	[2] (2014)
(Co, V) co-doped TiO_2(B) nanobelts[†]	265/239 mAh g^{-1} at 167.5 mA g^{-1}	256 mAh g^{-1} after 50 cycles at 167.5 mA g^{-1}	Not provided	[3] (2018)
Nb-doped TiO_2(B) thin films	273/208 mAh g^{-1} at 167.5 mA g^{-1}	115 mAh g^{-1} after 100 cycles at 16,750 mA g^{-1}		[4] (2013)
V-doped TiO_2(B) nanotubes	334/286 mAh g^{-1} at 150 mA g^{-1}	133 mAh g^{-1} after 100 cycles at 3000 mA g^{-1}	114 mAh g^{-1} at 6000 mA g^{-1}	[5] (2020)
Cu-doped TiO_2(B) nanowires	319/252 mAh g^{-1} at 167.5 mA g^{-1}	119 mAh g^{-1} after 2000 cycles at 2010 mA g^{-1}	51 mAh g^{-1} at 20,100 mA g^{-1}	[6] (2016)
Ni-doped TiO_2(B) nanobelts	254/189 mAh g^{-1} at 50 mA g^{-1}	173 mAh g^{-1} after 100 cycles at 50 mA g^{-1}	104 mAh g^{-1} at 1800 mA g^{-1}	[7] (2021)
C-doped TiO_2(B) nanowires	306/278 mAh g^{-1} at 33.5 mA g^{-1}	160 mAh g^{-1} after 1000 cycles at 3350 mA g^{-1}		[8] (2015)
P-doped TiO_2(B) nanowire arrays[*]	712/434 mAh g^{-1} at 167.5 mA g^{-1}	153 mAh g^{-1} after 3000 cycles at 3350 mA g^{-1}	141 mAh g^{-1} at 10,050 mA g^{-1}	[9] (2018)
N-doped TiO_2(B) nanosheets with N-doped graphene	583/479 mAh g^{-1} at 201 mA g^{-1}	338 mAh g^{-1} after 100 cycles at 201 mA g^{-1}	153 mAh g^{-1} at 16,750 mA g^{-1}	[10] (2016)
(N, B) co-doped TiO_2(B) nanotubes	399/276 mAh g^{-1} at 30 mA g^{-1}	140 mAh g^{-1} after 500 cycles at 12,000 mA g^{-1}		[11] (2015)

(Mn, F, N) co-doped TiO_2(B) nanotubes	358/244 mAh g^{-1} at 70 mA g^{-1}	232 mAh g^{-1} after 100 cycles at 70 mA g^{-1}	134 mAh g^{-1} at 1500 mA g^{-1}	This work (2023)

[#] The data are obtained in a narrow potential interval of 1.2–2.2 V.

[†] The cycling performance data are given in terms of charge (lithiation) capacity.

[*] The data are given for a wide potential range of 0.01–3.0 V.

Table S7. The fitting results for EIS spectra of electrodes based on undoped TiO_2 and TO-Mn/F/N-04 sample and the calculated lithium diffusion coefficient values

Sample	R_s (Ω)	R_f (Ω)	R_{ct} (Ω)	σ_W (Ω·$s^{-1/2}$)	D_{Li} (cm^2 s^{-1})
Undoped TiO_2	1.6	40.5	196.4	81.5	1.0×10^{-11}
TO-Mn/F/N-04	1.4	45.2	132.8	59.1	2.1×10^{-11}

References

1. Grosjean, R.; Fehse, M.; Pigeot-Remy, S.; Stievano, L.; Monconduit, L.; Cassaignon, S. Facile Synthetic Route towards Nanostructured Fe-TiO_2(B), Used as Negative Electrode for Li-Ion Batteries. *J. Power Sources* **2015**, *278*, 1–8, doi:10.1016/j.jpowsour.2014.12.032.
2. Zhang, K.; Katz, M.B.; Li, B.; Kim, S.J.; Du, X.; Hao, X.; Jokisaari, J.R.; Zhang, S.; Graham, G.W.; Van der Ven, A.; et al. Water-Free Titania-Bronze Thin Films with Superfast Lithium-Ion Transport. *Adv. Mater.* **2014**, *26*, 7365–7370, doi:10.1002/adma.201401757.
3. Amirsalehi, M.; Askari, M. Influence of Vanadium, Cobalt-Codoping on Electrochemical Performance of Titanium Dioxide Bronze Nanobelts Used as Lithium Ion Battery Anodes. *J. Mater. Sci. Mater. Electron.* **2018**, *29*, 13068–13076, doi:10.1007/s10854-018-9429-x.
4. Ventosa, E.; Mei, B.; Xia, W.; Muhler, M.; Schuhmann, W. TiO_2(B)/Anatase Composites Synthesized by Spray Drying as High Performance Negative Electrode Material in Li-Ion Batteries. *ChemSusChem* **2013**, *6*, 1312–1315, doi:10.1002/cssc.201300439.
5. Opra, D.P.; Gnedenkov, S.V.; Sokolov, A.A.; Podgorbunsky, A.B.; Ustinov, A.Y.; Mayorov, V.Y.; Kuryavyi, V.G.; Sinebryukhov, S.L. Vanadium-Doped TiO_2-B/Anatase Mesoporous Nanotubes with Improved Rate and Cycle Performance for Rechargeable Lithium and Sodium Batteries. *J. Mater. Sci. Technol.* **2020**, *54*, 181–189, doi:10.1016/j.jmst.2020.02.068.
6. Zhang, Y.; Meng, Y.; Zhu, K.; Qiu, H.; Ju, Y.; Gao, Y.; Du, F.; Zou, B.; Chen, G.; Wei, Y. Copper-Doped Titanium Dioxide Bronze Nanowires with Superior High Rate Capability for Lithium Ion Batteries. *ACS Appl. Mater. Interfaces* **2016**, *8*, 7957–7965, doi:10.1021/acsami.5b10766.
7. Opra, D.P.; Gnedenkov, S. V.; Sinebryukhov, S.L.; Gerasimenko, A. V.; Ziatdinov, A.M.; Sokolov, A.A.; Podgorbunsky, A.B.; Ustinov, A.Y.; Kuryavyi, V.G.; Mayorov, V.Y.; et al. Enhancing Lithium and Sodium Storage Properties of TiO_2(B) Nanobelts by Doping with Nickel and Zinc. *Nanomaterials* **2021**, *11*, 1703, doi:10.3390/nano11071703.
8. Goriparti, S.; Miele, E.; Prato, M.; Scarpellini, A.; Marras, S.; Monaco, S.; Toma, A.; Messina, G.C.; Alabastri, A.; Angelis, F. De; et al. Direct Synthesis of Carbon-Doped TiO_2-Bronze Nanowires as Anode Materials for High Performance Lithium-Ion Batteries. *ACS Appl. Mater. Interfaces* **2015**, *7*, 25139–25146, doi:10.1021/acsami.5b06426.
9. Cao, M.; Tao, L.; Lv, X.; Bu, Y.; Li, M.; Yin, H.; Zhu, M.; Zhong, Z.; Shen, Y.; Wang, M. Phosphorus-Doped TiO_2-B Nanowire Arrays Boosting Robust Pseudocapacitive Properties for Lithium Storage. *J. Power Sources* **2018**, *396*, 327–334, doi:10.1016/j.jpowsour.2018.06.012.
10. Han, Z.; Peng, J.; Liu, L.; Wang, G.; Yu, F.; Guo, X. Few-Layer TiO_2-B Nanosheets with N-Doped Graphene Nanosheets as a Highly Robust Anode for Lithium-Ion Batteries. *RSC Adv.* **2017**, *7*, 7864–7869, doi:10.1039/C6RA26929J.
11. Chen, C.; Hu, X.; Zhang, B.; Miao, L.; Huang, Y. Architectural Design and Phase Engineering of N/B-Codoped TiO_2(B)/Anatase Nanotube Assemblies for High-Rate and Long-Life Lithium Storage. *J. Mater. Chem. A* **2015**, *3*, 22591–22598, doi:10.1039/C5TA06884C.